JOURNAL OF COMPUTATIONAL PHYSICS **146,** 747–774 (1998)
ARTICLE NO. CP986082

Plane-Wave Analysis and Comparison of Split-Field, Biaxial, and Uniaxial PML Methods as ABCs for Pseudospectral Electromagnetic Wave Simulations in Curvilinear Coordinates

Baolin Yang*,[1] and Peter G. Petropoulos†

*Cadence Design Systems, Inc., 555 River Oaks Parkway, MS 3B1, San Jose, California 95134; †Department of Mathematics, New Jersey Institute of Technology, Newark, New Jersey 07102
E-mail: byang@cadence.com, pepetr@m.njit.edu

Received February 24, 1998; revised August 10, 1998

In this paper, we discuss and compare split-field, biaxial, and uniaxial perfectly matched layer (PML) methods for absorbing outgoing vector waves in cylindrical and spherical coordinates. We first extend Berenger's split-field formulation into spherical and cylindrical coordinates in such a way that it maintains all the desirable properties it exhibits in rectangular coordinates. Then we discuss the biaxial and the uniaxial medium PML methods in Cartesian coordinates and extend them to spherical and cylindrical coordinates. Properties of plane-wave solutions of the PML methods are analyzed. In particular, the decay and boundness properties of the solutions are considered in order to provide further insight into the different formulations presented herein. Moreover, we propose a set of symmetric hyperbolic equations for both the biaxial and the uniaxial PML methods in the time-domain, which is fine-tuned in numerical experiments and very suitable for time-domain problems. All three types of spherical and cylindrical PML methods are applied in simulations of plane wave scattering as well as radiating dipole problems. We use a multidomain pseudospectral (Chebyshev) numerical scheme, and the effectiveness of the PML methods is demonstrated through the accurate numerical results obtained. The order of outer-boundary reflection is as low as 0.1% of the exact solution.

Key Words: perfectly matched layer; pseudospectral method; multidomain method.

1. INTRODUCTION

In [1] Berenger proposed the perfectly matched layer (PML) method to truncate computational domains, used in the numerical solution of Maxwell's equations, without causing any reflection. The method was developed in Cartesian coordinates and the absorbing layer

0021-9991/98 $25.00

was shown to be nonreflecting at the rectangular vacuum-layer interface. It was extended into 3D in [2]. Recently, efforts have been seen to extend the rectangular PML methods into polar (2D), as well as spherical and cylindrical (3D) coordinate systems.

Unfortunately, some direct extensions of the split-field rectangular PML to cylindrical and spherical coordinates are not sufficiently justified, either theoretically or numerically [5, 14]. They are not reflectionless. As the split-field methods are still being used, we think that it is necessary to give extensions that are both theoretically and numerically justified. The split-field methods we propose and numerically tested attain this objective. Our methods are different from those recently proposed by Teixeira and Chew in [15]. The hyperbolic formulation of their methods also required a Berenger-like field splitting that is different from ours and were presented with no proof of the reflectionless property.

Also, the so-called uniaxial anisotropic medium (unsplit) rectangular PML methods [6–8] are extended to the coordinate systems considered herein. Extensions of these methods into other coordinate systems have also been attempted by many researchers. Kuzuoglu and Mittra presented [9] nonplanar absorbers for finite-element mesh truncation. They derived the reflection coefficients of their methods for spherical and cylindrical waves and showed that, in contrast to the rectangular true-PML method, the coefficients were no longer identically zero. The existence of ideally nonreflecting PML methods in spherical or cylindrical coordinate system remained unknown. In fact, the numerical results in [15] exhibit reflection up to 3%. In [16], the same authors obtained some different spherical and cylindrical PML methods, but no numerical results or comparison with the previous ones were given and, again, they did not prove their approach constituted a true PML.

Earlier [3], Yang *et al.* had already proposed a split-field PML method in polar coordinates (2D) which they applied to simulations of scattering by circular cylinders. That method was an extension of Berenger's rectangular PML. It was proven to be perfectly matched at the circular vacuum-layer interface while the superior accuracy of the method was demonstrated in numerical experiments. Further, [3] also discussed an alternative splitting, similar to that recently proposed in [15] and showed that its numerical results were substantially worse than the results of the proposed splitting. In the present paper, we continue with extensions of Berenger's rectangular PML into more 3D coordinate systems. We shall show that, like in [3], these extensions still retain the perfectly matched property of Berenger's rectangular PML method and we shall also present supporting numerical simulations. Indeed, going from methods in 2D polar coordinates [3] to methods in 3D cylindrical coordinates in the present paper is direct.

A nonsplit and well-posed ideally nonreflecting formulation of the PML method in polar coordinates was given in [4]. The efficacy of the method was demonstrated with numerical experiments. The present paper shall show that ideally nonreflecting unsplit PML methods can also be obtained in 3D spherical and cylindrical coordinate systems through the same approach for vector electromagnetic waves. A plane-wave analysis of the unsplit PML methods is given to demonstrate the point. More importantly, the proposed time-domain equations of the unsplit PML methods are symmetric hyperbolic. Although these PML methods are still extensions of the anisotropic medium rectangular PML [6–8] into other coordinate systems, the approach used to derive these extensions is different from that proposed in [16]. Due to the symmetry, well-posedness naturally follows from our formulation, which is not true for other formulations in general. We have also fine-tuned our formulation in numerical experiments and the proposed one in this paper is found to have the best accuracy and robustness.

Since our split and unsplit PML methods in cylindrical coordinates are straightforward extensions of our corresponding polar PML methods in 2D, our emphasis will be on the discussion of PML methods in spherical coordinates, where the split-field spherical PML, the biaxial spherical PML, and the uniaxial spherical PML will be analyzed and fully tested. We shall mainly discuss the plane-wave solutions of these PML methods and show the perfectly matched property and the decay of fields propagating in an arbitrary direction using plane waves.

For 3D spherical and cylindrical PML methods, the desired vacuum–layer interfaces are the surface of a sphere and the surface of a cylinder, respectively. The methods we develop admit plane-wave solutions that match perfectly at the vacuum–layer interface, i.e., any plane wave can pass through the interface without reflection. This is true for plane waves of any frequency and any incident angle. Decay properties are discussed for the split-field PML methods only. The split-field spherical PML method has the unique merit that plane wave of any incident angle decays in its propagation direction, which is true in the whole layer region. Split-field PML methods in other coordinate systems do not have this property and they usually depend on the corner regions for the complete absorption of waves. For the proposed unsplit PML methods (biaxial or uniaxial), since the additional scaling factors in the plane-wave solutions are only rational functions and the exponential decaying factor dominates the magnitude of the solutions, influence of the additional scaling factors on the decay properties of the solutions is limited. Here we want to emphasize that we have taken the propagation direction of plane waves into account in our analysis of the decay property. Reflection and field decay analysis (using cylindrical and spherical waves), and the proof that the uniaxial PML in cylindrical and spherical coordinates is a true PML can be found in [17]. The analysis approach herein is related to the analysis approach of [17] through the plane wave expansion of cylindrical and spherical waves and the addition theorem.

Numerical simulations of plane-wave scattering by a metal sphere and a radiating dipole are done to test the spherical PML methods. We also show a comparison of the split-field and uniaxial PML for a radiating dipole whose time variation is a step function that turns on and stays on for the duration of the simulation. Numerical simulations of scattering by a metal cylinder of finite length are also done to test the cylindrical PML methods. The numerical scheme we use is a multidomain pseudospectral (Chebyshev) scheme. The scheme is very accurate and as such it is a good choice in order to fully manifest the effects of PML methods in numerical experiments. For example, our numerical results suggest that the reflection of the spherical PML methods is as low as 0.1% of the exact solution.

The remainder of our paper is organized as follows. In Section 2, we give the non-dimensionalized 3D Maxwell's equations and its plane-wave solutions. In Section 3, we give the extensions of Berenger's PML methods into spherical and cylindrical coordinates. Section 4 discusses the biaxial and the uniaxial PML methods, first in rectangular, and then in spherical and cylindrical coordinates. In Section 5, numerical results validating the methods are presented, and concluding remarks are given in Section 6.

2. THE NONDIMENSIONALIZED MAXWELL'S EQUATIONS

We consider Maxwell's curl equations in free space:

$$\frac{\partial \tilde{H}}{\partial t} = -\frac{1}{\mu_0}\tilde{\nabla} \times \tilde{E}, \tag{1}$$

$$\frac{\partial \tilde{E}}{\partial t} = \frac{1}{\epsilon_0}\tilde{\nabla} \times \tilde{H}. \tag{2}$$

Here ε_0 and μ_0 are the free space permittivity and permeability, with the speed of light in free space being $\tilde{c} = (\varepsilon_0\mu_0)^{-1/2}$. To facilitate our analysis of PML methods, we scale the independent variables to nondimensionalize the above equations,

$$x = \tilde{x}/L, \quad y = \tilde{y}/L, \quad t = \tilde{c}\tilde{t}/L,$$

where L represents a length scale. Subsequently, the fields are normalized,

$$H = \tilde{H}, \quad E = \sqrt{\frac{\varepsilon_0}{\mu_0}}\tilde{E} = Z_0^{-1}\tilde{E},$$

where Z_0 represents the free-space impedance, and the nondimensionalized Maxwell's equations are obtained:

$$\frac{\partial H}{\partial t} = -\nabla \times E, \tag{3}$$

$$\frac{\partial E}{\partial t} = \nabla \times H. \tag{4}$$

We can write out the vector components of the curl operators in (3)–(4) and obtain a system of six coupled scalar equations. In three-dimensional spherical coordinates (r, θ, ϕ), we have

$$\frac{\partial E_r}{\partial t} = \frac{1}{r\sin\theta}\frac{\partial}{\partial \theta}(\sin\theta H_\phi) - \frac{1}{r\sin\theta}\frac{\partial H_\theta}{\partial \phi}, \tag{5}$$

$$\frac{\partial E_\theta}{\partial t} = \frac{1}{r\sin\theta}\frac{\partial H_r}{\partial \phi} - \frac{1}{r}\frac{\partial}{\partial r}(rH_\phi), \tag{6}$$

$$\frac{\partial E_\phi}{\partial t} = \frac{1}{r}\frac{\partial}{\partial r}(rH_\theta) - \frac{1}{r}\frac{\partial H_r}{\partial \theta}, \tag{7}$$

$$\frac{\partial H_r}{\partial t} = -\frac{1}{r\sin\theta}\frac{\partial}{\partial \theta}(\sin\theta E_\phi) + \frac{1}{r\sin\theta}\frac{\partial E_\theta}{\partial \phi}, \tag{8}$$

$$\frac{\partial H_\theta}{\partial t} = -\frac{1}{r\sin\theta}\frac{\partial E_r}{\partial \phi} + \frac{1}{r}\frac{\partial}{\partial r}(rE_\phi), \tag{9}$$

$$\frac{\partial H_\phi}{\partial t} = -\frac{1}{r}\frac{\partial}{\partial r}(rE_\theta) + \frac{1}{r}\frac{\partial E_r}{\partial \theta}. \tag{10}$$

In three-dimensional cylindrical coordinates (ρ, ϕ, z), we have

$$\frac{\partial E_\rho}{\partial t} = \frac{1}{\rho}\frac{\partial H_z}{\partial \phi} - \frac{\partial H_\phi}{\partial z}, \tag{11}$$

$$\frac{\partial E_\phi}{\partial t} = \frac{\partial H_\rho}{\partial z} - \frac{\partial H_z}{\partial \rho}, \tag{12}$$

$$\frac{\partial E_z}{\partial t} = \frac{1}{\rho}\frac{\partial \rho H_\phi}{\partial \rho} - \frac{1}{\rho}\frac{\partial H_\rho}{\partial \phi}. \tag{13}$$

To avoid repetition, we skip the governing equations for components of the magnetic fields. This rule is followed hereafter when appropriate.

Maxwell's equations admit the plane-wave solutions

$$E = (l_1\hat{x} + m_1\hat{y} + n_1\hat{z})\, e^{i\omega(t-lx-my-nz)}, \tag{14}$$

$$H = (l_2\hat{x} + m_2\hat{y} + n_2\hat{z})\, e^{i\omega(t-lx-my-nz)}, \tag{15}$$

where

$$l_1\hat{x} + m_1\hat{y} + n_1\hat{z} = (l_2\hat{x} + m_2\hat{y} + n_2\hat{z}) \times (l\hat{x} + m\hat{y} + n\hat{z}), \tag{16}$$

$$l_2\hat{x} + m_2\hat{y} + n_2\hat{z} = (l\hat{x} + m\hat{y} + n\hat{z}) \times (l_1\hat{x} + m_1\hat{y} + n_1\hat{z}). \tag{17}$$

For a plane wave incident in the direction θ_0, ϕ_0, we have

$$e^{i\omega(t-lx-my-nz)} = e^{i\omega(t - r(\cos\theta_0\cos\theta + \sin\theta_0\sin\theta\cos(\phi-\phi_0)))}. \tag{18}$$

in the spherical coordinate system and

$$e^{i\omega(t-lx-my-nz)} = e^{i\omega\left(t - \sqrt{1-n^2}\rho\cos(\phi-\phi_0) - nz\right)} \tag{19}$$

in the cylindrical coordinate system.

The plane-wave field components in spherical coordinates are given as

$$E_r = (\cos\phi\sin\theta l_1 + \sin\phi\sin\theta m_1 + \cos\theta n_1)\, e^{i\omega(t - r(\cos\theta_0\cos\theta + \sin\theta_0\sin\theta\cos(\phi-\phi_0)))}, \tag{20}$$

$$E_\theta = (\cos\phi\cos\theta l_1 + \sin\phi\cos\theta m_1 - \sin\theta n_1)\, e^{i\omega(t - r(\cos\theta_0\cos\theta + \sin\theta_0\sin\theta\cos(\phi-\phi_0)))}, \tag{21}$$

$$E_\phi = (-\sin\phi l_1 + \cos\phi m_1)\, e^{i\omega(t - r(\cos\theta_0\cos\theta + \sin\theta_0\sin\theta\cos(\phi-\phi_0)))}, \tag{22}$$

and the plane-wave field components in cylindrical coordinates as

$$E_\rho = (\cos\phi l_1 + \sin\phi m_1)\, e^{i\omega\left(t - \sqrt{1-n^2}\rho\cos(\phi-\phi_0) - nz\right)}, \tag{23}$$

$$E_\phi = (-\sin\phi l_1 + \cos\phi m_1)\, e^{i\omega\left(t - \sqrt{1-n^2}\rho\cos(\phi-\phi_0) - nz\right)}, \tag{24}$$

$$E_z = n_1\, e^{i\omega\left(t - \sqrt{1-n^2}\rho\cos(\phi-\phi_0) - nz\right)}. \tag{25}$$

These plane-wave solutions are to be perfectly matched to decaying plane-wave solutions in the absorbing layer.

3. EXTENSIONS OF BERENGER'S PML METHODS

In this section, we present the extensions of Berenger's PML methods to spherical and cylindrical coordinates. The plane-wave solutions of these PML methods are simpler than those of the unsplit methods which will be given in Section 4. We shall also prove that plane-wave solutions in the spherical PML decay in all directions of propagation.

In the following, we first explain Berenger's PML method with a varying conductivity parameter and analyze its plane-wave solutions. Then we present our spherical and cylindrical PML methods and analyze their decay property in the direction of wave propagation. We have found in our work that this property is important for the success of PML methods. In any numerical computation, there are numerical reflections at the outer boundaries of the

PML due to the inexact boundary conditions applied there and one wants those reflected waves, although of very small magnitude, to be further absorbed as they propagate back towards the interior region.

3.1. *Berenger's Perfectly Matched Layer*

In [1] Berenger gave the perfectly matched layer method suitable for rectangular grid truncation and wave absorption. Here we give a simplified plane-wave analysis of the method, where we consider a layer of continuously varying absorption strength.

Our approach is to obtain the equations that admit plane-wave solutions with a frequency-independent decay factor of the following form:

$$D(x, y, z) = e^{-l\sigma_x(x) - m\sigma_y(y) - n\sigma_z(z)}. \tag{26}$$

We then have the split-field PML system in Cartesian coordinates,

$$\frac{\partial E_{xy}}{\partial t} = \frac{\partial (H_{zx} + H_{zy})}{\partial y} - \sigma_y'(y) E_{xy}, \tag{27}$$

$$\frac{\partial E_{xz}}{\partial t} = -\frac{\partial (H_{yx} + H_{yz})}{\partial z} - \sigma_z'(z) E_{xz}, \tag{28}$$

$$\frac{\partial E_{yz}}{\partial t} = \frac{\partial (H_{xy} + H_{xz})}{\partial z} - \sigma_z'(z) E_{yz}, \tag{29}$$

$$\frac{\partial E_{yx}}{\partial t} = -\frac{\partial (H_{zx} + H_{zy})}{\partial x} - \sigma_x'(x) E_{yx}, \tag{30}$$

$$\frac{\partial E_{zx}}{\partial t} = \frac{\partial (H_{yx} + H_{yz})}{\partial x} - \sigma_x'(x) E_{zx}, \tag{31}$$

$$\frac{\partial E_{zy}}{\partial t} = -\frac{\partial (H_{xy} + H_{xz})}{\partial y} - \sigma_y'(y) E_{zy}, \tag{32}$$

that admits the following decaying plane-wave solutions:

$$E_{xy} = -n_2 m\, e^{i\omega(t - xl - ym - nz)} D(x, y, z), \tag{33}$$

$$E_{xz} = m_2 n\, e^{i\omega(t - xl - ym - nz)} D(x, y, z), \tag{34}$$

$$E_{yz} = -l_2 n\, e^{i\omega(t - xl - ym - nz)} D(x, y, z), \tag{35}$$

$$E_{yx} = n_2 l\, e^{i\omega(t - xl - ym - nz)} D(x, y, z), \tag{36}$$

$$E_{zx} = -m_2 l\, e^{i\omega(t - xl - ym - nz)} D(x, y, z), \tag{37}$$

$$E_{zy} = l_2 m\, e^{i\omega(t - xl - ym - nz)} D(x, y, z). \tag{38}$$

According to the relations (16)–(17) that couple (l, m, n), (l_1, m_1, n_1), and (l_2, m_2, n_2), we have $E_{xy} + E_{xz} = E_x D(x, y, z)$, $E_{yz} + E_{yx} = E_y D(x, y, z)$, and $E_{zx} + E_{zy} = E_z D(x, y, z)$, where E_x, E_y, and E_z are the plane-wave solutions in Eq. (14). So the decaying plane-wave solutions in the layer region match perfectly with the plane-wave solutions in a vacuum if we let $\sigma_x(x)$, $\sigma_y(y)$, and $\sigma_z(z)$ approach zero smoothly enough when (x, y, z) approaches the vacuum–layer interface from the layer side.

3.2. *Spherical Perfectly Matched Layer*

In this section we propose a split-field spherical PML method. We use the method to terminate spherical computational domains and the vacuum–layer interface is a sphere. We prove that plane waves of any incident direction and any frequency pass the vacuum–layer interface without causing any reflection and decay in all directions of propagation in the layer region independently of the frequency. The absorption in the layer only varies with the radius r, and it approaches zero smoothly towards the interface.

In designing such a perfectly matched layer, we split the original equations and add low-order absorbing terms (see undifferentiated terms below). Our approach is an extension of the idea of Berenger's PML method to spherical coordinates, rather than a direct translation of Berenger's PML equations to spherical coordinates (which *does not* result in a true PML). We have found that it is not necessary to split the $\hat{r}$ component of the fields as the E_r and H_r components are never tangential to a PML region. This is in contrast to the situation in cylindrical coordinates (see Section 3.3).

In deriving the spherical PML method, our objective is to obtain differential equations that admit plane-wave solutions with a decaying factor of the form

$$D(r,\theta,\phi) = e^{-\sigma_r(r)(\cos\theta_0\cos\theta + \sin\theta_0\sin\theta\cos(\phi-\phi_0))}. \tag{39}$$

We obtain the following split-field formulation of Maxwell's equations in the layer:

$$\frac{\partial E_r}{\partial t} = \frac{1}{r\sin\theta}\frac{\partial}{\partial\theta}(\sin\theta(H_{\phi r} + H_{\phi\theta})) - \frac{1}{r\sin\theta}\frac{\partial(H_{\theta\phi} + H_{\theta r})}{\partial\phi} - \frac{\sigma_r(r)}{r}E_r, \tag{40}$$

$$\frac{\partial E_{\theta\phi}}{\partial t} = \frac{1}{r\sin\theta}\frac{\partial H_r}{\partial\phi} - \frac{1}{r}(H_{\phi r} + H_{\phi\theta}) - \frac{\sigma_r(r)}{r}E_{\theta\phi}, \tag{41}$$

$$\frac{\partial E_{\theta r}}{\partial t} = -\frac{\partial(H_{\phi r} + H_{\phi\theta})}{\partial r} - \sigma_r'(r)E_{\theta r}, \tag{42}$$

$$\frac{\partial E_{\phi r}}{\partial t} = \frac{\partial(H_{\theta\phi} + H_{\theta r})}{\partial r} - \sigma_r'(r)E_{\phi r}, \tag{43}$$

$$\frac{\partial E_{\phi\theta}}{\partial t} = -\frac{1}{r}\frac{\partial H_r}{\partial\theta} + \frac{1}{r}(H_{\theta\phi} + H_{\theta r}) - \frac{\sigma_r(r)}{r}E_{\phi\theta}. \tag{44}$$

We note that one only needs to solve 10 equations, of which we just give five in the above, compared with 12 equations one needs to solve for the split-field rectangular PML method. We also note that in [15], six additional field components are needed inside the PML. In [15], the reflection of the spherical PML is 0.8% of the maximum amplitude of the simulated pulse. The methods are similar in nature in the frequency domain, and the approaches [15] require a splitting of the fields to give a PML for transient waves. However, no split-field time-domain formulation was given in [15] and we had shown in [3] that having the right split-field formulation is important.

Let the vacuum-layer interface be at $r = r_0$. We require that $\sigma_r(r) = 0$ for $r \le r_0$ for the decaying plane waves in the PML to match incident plane waves perfectly. The function $\sigma_r(r)$ must satisfy the requirements

$$\sigma_r(r_0) = 0 \tag{45}$$

and

$$\sigma_r(r) > 0 \quad \text{for } r > r_0, \tag{46}$$

so that the plane-wave solutions decay for $r > r_0$. We also require that

$$\sigma_r'(r) > 0 \quad \text{for } r > r_0. \tag{47}$$

An example of a valid choice for $\sigma_r(r)$ is

$$\sigma_r(r) = C(r - r_0)^n, \quad n = 1, 2, \ldots; r \geq r_0, \tag{48}$$

where C is a positive constant. This family of functions satisfies the requirements in (45)–(47).

The split-field PML equations admit the following set of plane-wave solutions with the desired decaying factor:

$$E_r = (\cos\phi \sin\theta l_1 + \sin\phi \sin\theta m_1 + \cos\theta n_1)\, e^{i\omega(t - r(\cos\theta_0 \cos\theta + \sin\theta_0 \sin\theta \cos(\phi - \phi_0)))} D(r, \theta, \phi), \tag{49}$$

$$E_{\theta\phi} = (\cos\phi \sin\theta l_2 + \sin\phi \sin\theta m_2 + \cos\theta n_2) \sin\theta_0 \sin(\phi - \phi_0) \times e^{i\omega(t - r(\cos\theta_0 \cos\theta + \sin\theta_0 \sin\theta \cos(\phi - \phi_0)))} D(r, \theta, \phi), \tag{50}$$

$$E_{\theta r} = (-\sin\phi l_2 + \cos\phi m_2)(\cos\theta_0 \cos\theta + \sin\theta_0 \sin\theta \cos(\phi - \phi_0)) \times e^{i\omega(t - r(\cos\theta_0 \cos\theta + \sin\theta_0 \sin\theta \cos(\phi - \phi_0)))} D(r, \theta, \phi), \tag{51}$$

$$E_{\phi r} = -(\cos\phi \cos\theta l_2 + \sin\phi \cos\theta m_2 - \sin\theta n_2)(\cos\theta_0 \cos\theta + \sin\theta_0 \sin\theta \cos(\phi - \phi_0)) \times e^{i\omega(t - r(\cos\theta_0 \cos\theta + \sin\theta_0 \sin\theta \cos(\phi - \phi_0)))} D(r, \theta, \phi), \tag{52}$$

$$E_{\phi\theta} = -(\cos\phi \sin\theta l_2 + \sin\phi \sin\theta m_2 + \cos\theta n_2)(\cos\theta_0 \sin\theta - \sin\theta_0 \cos\theta \cos(\phi - \phi_0)) \times e^{i\omega(t - r(\cos\theta_0 \cos\theta + \sin\theta_0 \sin\theta \cos(\phi - \phi_0)))} D(r, \theta, \phi), \tag{53}$$

where (l_2, m_2, n_2), (l_1, m_1, n_1), and (l, m, n) satisfy (16)–(17). Note that now we have $l = \cos\phi_0 \sin\theta_0$, $m = \sin\phi_0 \sin\theta_0$, and $n = \cos\theta_0$. One can verify that

$$\begin{aligned} E_{\theta\phi} + E_{\theta r} &= \big[(\cos\phi \sin\theta l_2 + \sin\phi \sin\theta m_2 + \cos\theta n_2) \sin\theta_0 \sin(\phi - \phi_0) \\ &\quad + (-\sin\phi l_2 + \cos\phi m_2)(\cos\theta_0 \cos\theta + sin\theta_0 \sin\theta \cos(\phi - \phi_0)) \\ &\quad \times e^{i\omega(t - r(\cos\theta_0 \cos\theta + \sin\theta_0 \sin\theta \cos(\phi - \phi_0)))} D(r, \theta, \phi) \\ &= (\cos\phi \cos\theta l_1 + \sin\phi \cos\theta m_1 - \sin\theta n_1)\big] \\ &\quad \times e^{i\omega(t - r(\cos\theta_0 \cos\theta + \sin\theta_0 \sin\theta \cos(\phi - \phi_0)))} D(r, \theta, \phi) \\ &= E_\theta D(r, \theta, \phi), \end{aligned} \tag{54}$$

and, similarly, one can also verify that

$$E_{\phi r} + E_{\phi\theta} = E_\phi D(r, \theta, \phi), \tag{55}$$

by applying the relations (16)–(17) that couple (l, m, n), (l_1, m_1, n_1), and (l_2, m_2, n_2), where E_ϕ, E_θ are the plane-wave solutions in Eqs. (20)–(22). Hence, at the vacuum–layer interface,

where $\sigma_r(r) = 0$, the decaying plane waves E_r, $E_{\theta\phi} + E_{\theta r}$, and $E_{\phi r} + E_{\phi\theta}$ match the plane-wave solutions E_r, E_θ, and E_ϕ in free-space perfectly. Note that this is true for plane waves of any frequency and any incident angle.

It is not straightforward to understand the decay property of the plane-wave solutions in the layer by looking at the decay factor $e^{-\sigma_r(r)(\cos\theta_0\cos\theta+\sin\theta_0\sin\theta\cos\phi-\phi_0))}$. In order to get a clear picture of the rate of change of the magnitude of the wave, one must analyze the directional derivative of the decay factor.

LEMMA 3.1. *Let* $\mathbf{l} = (\cos\phi_0\sin\theta_0, \sin\phi_0\sin\theta_0, \cos\theta_0)$ *be the normalized wave vector and assume that* $\sigma_r(r)$ *satisfies the conditions* (46)–(47). *Then all plane waves decay in the direction of propagation as*

$$\frac{\partial D(r,\theta,\phi)}{\partial \mathbf{l}} = \frac{\partial e^{-\sigma_r(r)(\cos\theta_0\cos\theta+\sin\theta_0\sin\theta\cos(\phi-\phi_0))}}{\partial \mathbf{l}} < 0, \tag{56}$$

when $r > r_0$ *for any* ϕ_0 *and* θ_0.

Proof.

$$\begin{aligned}
&\frac{\partial D(r,\theta,\phi)}{\partial \mathbf{l}}\\
&= \cos\phi_0\sin\theta_0\frac{\partial D(r,\theta,\phi)}{\partial x} + \sin\phi_0\sin\theta_0\frac{\partial D(r,\theta,\phi)}{\partial y} + \cos\theta_0\frac{\partial D(r,\theta,\phi)}{\partial z}\\
&= \cos\phi_0\sin\theta_0\cos\phi\sin\theta\frac{\partial D(r,\theta,\phi)}{\partial r} - \cos\phi_0\sin\theta_0\frac{\sin\phi}{r\sin\theta}\frac{\partial D(r,\theta,\phi)}{\partial \phi}\\
&\quad + \cos\phi_0\sin\theta_0\frac{\cos\phi\cos\theta}{r}\frac{\partial D(r,\theta,\phi)}{\partial \theta}\\
&\quad + \sin\phi_0\sin\theta_0\sin\phi\sin\theta\frac{\partial D(r,\theta,\phi)}{\partial r} + \sin\phi_0\sin\theta_0\frac{\cos\phi}{r\sin\theta}\frac{\partial D(r,\theta,\phi)}{\partial \phi}\\
&\quad + \sin\phi_0\sin\theta_0\frac{\sin\phi\cos\theta}{r}\frac{\partial D(r,\theta,\phi)}{\partial \theta}\\
&\quad + \cos\theta_0\cos\theta\frac{\partial D(r,\theta,\phi)}{\partial r} - \cos\theta_0\frac{\sin\theta}{r}\frac{\partial D(r,\theta,\phi)}{\partial \theta}\\
&= (\sin\theta_0\sin\theta\cos(\phi-\phi_0) + \cos\theta_0\cos\theta)\frac{\partial D(r,\theta,\phi)}{\partial r}\\
&\quad - \sin\theta_0\sin(\phi-\phi_0)\frac{1}{r\sin\theta}\frac{\partial D(r,\theta,\phi)}{\partial \phi}\\
&\quad + (\sin\theta_0\cos\theta\cos(\phi-\phi_0) - \cos\theta_0\sin\theta)\frac{1}{r}\frac{\partial D(r,\theta,\phi)}{\partial \theta}\\
&= -\Bigg[(\sin\theta_0\sin\theta\cos(\phi-\phi_0) + \cos\theta_0\cos\theta)^2\sigma_r'(r) + (\sin\theta_0\sin(\phi-\phi_0))^2\frac{\sigma_r(r)}{r}\\
&\quad + (\sin\theta_0\cos\theta\cos(\phi-\phi_0) - \cos\theta_0\sin\theta)^2\frac{\sigma_r(r)}{r}\Bigg]D(r,\theta,\phi).
\end{aligned}$$

Hence we have

$$\frac{\partial D(r,\theta,\phi)}{\partial \mathbf{l}} = \frac{\partial e^{-\sigma_r(r)(\cos\theta_0\cos\theta+\sin\theta_0\sin\theta\cos(\phi-\phi_0))}}{\partial \mathbf{l}} < 0$$

for any ϕ_0 and θ_0. ■

The lemma shows that all plane waves entering the PML decay exponentially along any direction of propagation inside the layer. In an actual computation, the PML does not extend to infinity and there will be reflections from the outer boundary of the PML region. In this case, the decay relation (56) still holds for the reflected waves. Thus, the reflected waves get further attenuated along the way back towards the computational domain. Note that reflected waves, even numerical reflections, can be expanded in plane waves locally. This is the reason for the success of the PML methods. Since

$$(\sin\theta_0 \sin\theta \cos(\phi-\phi_0) + \cos\theta_0 \cos\theta)^2 \sigma_r'(r) + (\sin\theta_0 \sin(\phi-\phi_0))^2 \frac{\sigma_r(r)}{r}$$
$$+ (\sin\theta_0 \cos\theta \cos(\phi-\phi_0) - \cos\theta_0 \sin\theta)^2 \frac{\sigma_r(r)}{r} \geq min\left(\sigma_r'(r), \frac{\sigma_r(r)}{r}\right) > 0 \quad (57)$$

for $r > r_0$, we have a lower bound for the rate of decay regardless of the direction of wave propagation ϕ_0 and θ_0 in the layer region away from the interface. We emphasize that we cannot find such a lower bound for the PML in Cartesian coordinates.

3.3. *Cylindrical Perfectly Matched Layer*

It is also desirable to have a perfectly matched layer method in cylindrical coordinates. Here the vacuum–layer interface is required to be at $\rho = \rho_0$ and $|z| = z_0$, where ρ_0 and z_0 are constants. For this purpose, we can apply the polar perfectly matched layer [3] in the $\rho - \phi$ plane and apply rectangular perfectly matched layer method in the z-direction.

Our objective is to obtain the equations that admit plane-wave solutions with the decay factor:

$$D(\rho, \phi, z) = e^{-\sigma_\rho(\rho)\sqrt{1-n^2}\cos(\phi-\phi_0) - \sigma_z(z)nz}. \quad (58)$$

With the split-field approach, we need to solve the following equations:

$$\frac{\partial E_{\rho z}}{\partial t} = -\frac{\partial (H_{\phi z} + H_{\phi\rho})}{\partial z} - \sigma_z'(z) E_{\rho z}, \quad (59)$$

$$\frac{\partial E_{\rho\phi}}{\partial t} = \frac{1}{\rho}\frac{\partial (H_{z\rho} + H_{z\phi})}{\partial \phi} - \frac{\sigma_\rho(\rho)}{\rho} E_{\rho\phi}, \quad (60)$$

$$\frac{\partial E_{\phi z}}{\partial t} = \frac{\partial (H_{\rho z} + H_{\rho\phi})}{\partial z} - \sigma_z'(z) E_{\phi z}, \quad (61)$$

$$\frac{\partial E_{\phi\rho}}{\partial t} = -\frac{\partial (H_{z\rho} + H_{z\phi})}{\partial \rho} - \sigma_\rho'(\rho) E_{\phi\rho}, \quad (62)$$

$$\frac{\partial E_{z\rho}}{\partial t} = \frac{\partial (H_{\phi z} + H_{\phi\rho})}{\partial \rho} - \sigma_\rho'(\rho) E_{z\rho}, \quad (63)$$

$$\frac{\partial E_{z\phi}}{\partial t} = -\frac{1}{\rho}\frac{\partial (H_{\rho z} + H_{\rho\phi})}{\partial \phi} + \frac{H_{\phi z} + H_{\phi\rho}}{\rho} - \frac{\sigma_\rho(\rho)}{\rho} E_{z\phi}. \quad (64)$$

We note that in [15], although it was tested in 3D, the equations for the cylindrical PML was actually given in 2D and the method was similar to Navarro's method [14] already

discussed in [3]. Unfortunately, Navarro's method was shown to have a poorer performance than our method [3], which might be the reason for the substantial 3% reflection seen in [15]. The important thing to notice is that the term $(H_{\phi z} + H_{\phi\rho})/\rho$ is in Eq. (64) rather than in Eq. (63).

Let the vacuum-layer interface be at $\rho = \rho_0$ and $|z| = z_0$. We should require that $\sigma_\rho(\rho) = 0$ for $\rho < \rho_0$ and $\sigma_z(z) = 0$ for $|z| < z_0$ in order for the decaying plane waves in the PML to match incident plane waves perfectly. Following the considerations of the absorbing and reflectionless properties of the polar PML method, $\sigma_\rho(\rho)$ and $\sigma_z(z)$ must satisfy the requirements:

$$\sigma_\rho(\rho_0) = 0, \quad \sigma_z(z)|_{|z|=z_0} = 0, \tag{65}$$

and

$$\sigma_\rho(\rho) > 0 \quad \text{for } \rho > \rho_0, \quad \sigma_z(z) > 0 \quad \text{for } |z| > z_0, \tag{66}$$

so that the plane-wave solutions decay for $\rho > \rho_0$ or $|z| > z_0$. We also require that

$$\sigma'_\rho(\rho) > 0 \quad \text{for } \rho > \rho_0, \quad \sigma'_z(z) > 0 \quad \text{for } |z| > z_0. \tag{67}$$

An example of a valid choice of $\sigma_\rho(r)$ and $\sigma_z(z)$ is

$$\sigma_\rho(\rho) = C(\rho - \rho_0)^n, \quad n = 1, 2, \ldots; \rho \geq \rho_0, \tag{68}$$

$$\sigma_z(z) = C(|z| - z_0)^n, \quad n = 1, 2, \ldots; |z| \geq z_0, \tag{69}$$

where C is a positive constant. This family of functions satisfies the requirements in (65)–(67).

For the cylindrical perfectly matched layer method, it can be verified that we have the following decaying plane-wave solutions:

$$E_{\rho z} = (-\sin\phi l_2 + \cos\phi m_2) n\, e^{i\omega\left(t - \rho\sqrt{1-n^2}\cos(\phi-\phi_0) - zn\right)} D(\rho, \phi, z), \tag{70}$$

$$E_{\rho\phi} = n_2 \sin(\phi - \phi_0)\sqrt{1-n^2}\, e^{i\omega\left(t - \rho\sqrt{1-n^2}\cos(\phi-\phi_0) - zn\right)} D(\rho, \phi, z), \tag{71}$$

$$E_{\phi z} = -(\cos\phi l_2 + \sin\phi m_2) n\, e^{i\omega\left(t - \rho\sqrt{1-n^2}\cos(\phi-\phi_0) - zn\right)} D(\rho, \phi, z), \tag{72}$$

$$E_{\phi\rho} = n_2 \cos(\phi - \phi_0)\sqrt{1-n^2}\, e^{i\omega\left(t - \rho\sqrt{1-n^2}\cos(\phi-\phi_0) - zn\right)} D(\rho, \phi, z), \tag{73}$$

$$E_{z\rho} = -(-\sin\phi l_2 + \cos\phi m_2)\cos(\phi - \phi_0)\sqrt{1-n^2}\, e^{i\omega\left(t - \rho\sqrt{1-n^2}\cos(\phi-\phi_0) - zn\right)} D(\rho, \phi, z), \tag{74}$$

$$E_{z\phi} = -(\cos\phi l_2 + \sin\phi m_2)\sin(\phi - \phi_0)\sqrt{1-n^2}\, e^{i\omega\left(t - \rho\sqrt{1-n^2}\cos(\phi-\phi_0) - zn\right)} D(\rho, \phi, z), \tag{75}$$

where (l_2, m_2, n_2), (l_1, m_1, n_1), and (l, m, n) satisfy relations (16)–(17). Note that now we

have $l = \sqrt{1-n^2}\cos\phi_0$, $m = \sqrt{1-n^2}\sin\phi_0$, and $n = n$. One can verify that

$$\begin{aligned} E_{z\rho} + E_{z\phi} &= -((-\sin\phi l_2 + \cos\phi m_2)\cos(\phi-\phi_0) + (\cos\phi l_2 + \sin\phi m_2) \\ &\quad \times \sin(\phi-\phi_0))\sqrt{1-n^2}\, e^{i\omega(t-\rho\cos(\phi-\phi_0)-zn)} D(\rho,\phi,z) \\ &= -(-\sin\phi_0 l_2 + \cos\phi_0 m_2)\sqrt{1-n^2}\, e^{i\omega(t-\rho\cos(\phi-\phi_0)-zn)} D(\rho,\phi,z) \\ &= n_1\, e^{i\omega\left(t-\rho\sqrt{1-n^2}\cos(\phi-\phi_0)-zn\right)} D(\rho,\phi,z) \\ &= E_z D(\rho,\phi,z), \end{aligned} \tag{76}$$

and, similarly, one can also verify that

$$E_{\rho z} + E_{\rho\phi} = E_\rho D(\rho,\phi,z), \tag{77}$$

$$E_{\phi z} + E_{\phi\rho} = E_\phi D(\rho,\phi,z), \tag{78}$$

by applying the relations (16)–(17) that couple (l, m, n), (l_1, m_1, n_1), and (l_2, m_2, n_2), where E_ρ, E_ϕ, and E_z are plane-wave solutions in Eqs. (23)–(25). Hence, at the vacuum-layer interface, where $\sigma_\rho(\rho) = \sigma_z(z) = 0$, the decaying plane waves $E_{\rho z} + E_{\rho\phi}$, $E_{\phi z} + E_{\phi\rho}$, and $E_{z\rho} + E_{z\phi}$ match the plane-wave solutions E_ρ, E_ϕ, and E_z in free-space perfectly. Note that this is true for plane waves of any frequency and any incident angle.

We can also analyze the directional derivative of the decaying factor to get a clear picture of the rate of change of the magnitude of the plane waves. The analysis is a straightforward extension of the 2D polar PML analysis given in [3]. Here we only give the result.

LEMMA 3.2. *Let* $\mathbf{l} = (\sqrt{1-n^2}\cos\phi_0, \sqrt{1-n^2}\sin\phi_0, n)$ *be the normalized wave vector and assume that* $\sigma_\rho(\rho)$ *and* $\sigma_z(z)$ *satisfies the conditions* (46)–(47). *Then plane waves do not increase in all directions of propagation as*

$$\frac{\partial D(\rho,\phi,z)}{\partial \mathbf{l}} = \frac{\partial e^{-\sigma_\rho(\rho)\cos(\phi-\phi_0)-\sigma_z(z)z}}{\partial \mathbf{l}} \le 0, \tag{79}$$

when $\rho > \rho_0$ *or* $|z| > z_0$ *for any* ϕ_0 *and* n.

The decay property of the cylindrical PML is shared by both the rectangular and polar PML methods [3]. It is only in two special cases that plane-wave solutions do not decay in the PML, i.e., when plane waves propagate in the z-direction and in the region $\rho > \rho_0$ and $|z| \le z_0$, or when plane waves propagate in the direction orthogonal to z and in the region $\rho \le \rho_0$ and $|z| > z_0$. The corner regions, $\rho > \rho_0$ and $|z| > z_0$, are important for all plane waves to be absorbed. However, the situation here is much less severe than that for the rectangular PML method.

4. THE BIAXIAL AND THE UNIAXIAL PML METHODS

Since Berenger first presented the split-field PML method, efforts have been made to modify the method and obtain unsplit PML methods. Besides from the latter methods' being computationally more efficient, the efforts are worthwhile since the split-field rectangular PML equations are only weakly well-posed and may suffer from instability problems, as shown in [11].

The unsplit PML methods we present in this section modify Maxwell's equations by adding low-order (undifferentiated) source terms that satisfy ordinary differential equations. Hence the governing equations are symmetric hyperbolic and strongly well-posed just like the original Maxwell's equations. The plane-wave solutions now have additional scaling factors which depend on the frequency, ω. This additional degree of freedom makes it possible to design the unsplit-field PML methods.

4.1. *The Perfectly Matched Anisotropic Medium*

In [6] a PML method using an anisotropic lossy uniaxial medium was presented and was applied to frequency-domain-based finite-element methods. The works [7, 8] implemented the uniaxial medium as a PML for the FD-TD algorithm. The constitutive parameters of this anisotropic medium are given in terms of the complex permittivity and permeability tensors $\overline{\overline{\epsilon}} = \epsilon_0[\Lambda]$ and $\overline{\overline{\mu}} = \mu_0[\Lambda]$, where $[\Lambda]$ is the diagonal matrix,

$$[\Lambda] = \begin{bmatrix} 1 + \frac{\sigma_z'(z)}{i\omega} & 0 & 0 \\ 0 & 1 + \frac{\sigma_z'(z)}{i\omega} & 0 \\ 0 & 0 & \frac{1}{1+\frac{\sigma_z'(z)}{i\omega}} \end{bmatrix}, \tag{80}$$

that represents a uniaxial medium in the $\hat{z}$-direction. In the uniaxial medium, the nondimensionalized Ampere's law can be expressed in matrix form as

$$\begin{bmatrix} \frac{\partial H_z}{\partial y} - \frac{\partial H_y}{\partial z} \\ \frac{\partial H_x}{\partial z} - \frac{\partial H_z}{\partial x} \\ \frac{\partial H_y}{\partial x} - \frac{\partial H_x}{\partial y} \end{bmatrix} = i\omega[\Lambda] \begin{bmatrix} E_x \\ E_y \\ E_z \end{bmatrix}. \tag{81}$$

It was shown in the original papers that the above equations admit the plane-wave solutions

$$E = \left(l_1 \hat{x} + m_1 \hat{y} + n_1 \left(1 + \frac{\sigma_z'(z)}{i\omega} \right) \hat{z} \right) e^{i\omega(t - lx - my - nz)} e^{-\sigma_z(z)n}, \tag{82}$$

$$H = \left(l_2 \hat{x} + m_2 \hat{y} + n_2 \left(1 + \frac{\sigma_z'(z)}{i\omega} \right) \hat{z} \right) e^{i\omega(t - lx - my - nz)} e^{-\sigma_z(z)n}, \tag{83}$$

where (l, m, n), (l_1, m_1, n_1), and (l_2, m_2, n_2) are coupled by the relations (16)–(17). The above solutions are unbounded as $\omega \to 0$, which is certainly unphysical.

However, we can design a layer that has the plane-wave solutions

$$E = \left(l_1 \frac{i\omega}{\sigma_z'(z) + i\omega} \hat{x} + m_1 \frac{i\omega}{\sigma_z'(z) + i\omega} \hat{y} + n_1 \hat{z} \right) e^{i\omega(t - lx - my - nz)} \, e^{-\sigma_z(z)n}, \tag{84}$$

$$H = \left(l_2 \frac{i\omega}{\sigma_z'(z) + i\omega} \hat{x} + m_2 \frac{i\omega}{\sigma_z'(z) + i\omega} \hat{y} + n_2 \hat{z} \right) e^{i\omega(t - lx - my - nz)} \, e^{-\sigma_z(z)n}, \tag{85}$$

where (l, m, n), (l_1, m_1, n_1), and (l_2, m_2, n_2) are coupled by the relations (16)–(17). The magnitude of this set of plane-wave solutions are uniformly bounded. It can be verified that

they are the solutions of the following equations:

$$\begin{bmatrix} \frac{\partial H_z}{\partial y} - \frac{\partial H_y}{\partial z} \\ \frac{\partial H_x}{\partial z} - \frac{\partial H_z}{\partial x} \\ \frac{\partial H_y}{\partial x} - \frac{\partial H_x}{\partial y} \end{bmatrix} + \begin{bmatrix} \frac{\sigma_z''(z)}{\sigma_z'(z)+i\omega} H_y \\ -\frac{\sigma_z''(z)}{\sigma_z'(z)+i\omega} H_x \\ 0 \end{bmatrix} = i\omega[\Lambda] \begin{bmatrix} E_x \\ E_y \\ E_z \end{bmatrix}. \tag{86}$$

Note that Eq. (86) implies the biaxial constitutive law $D = [\Lambda] \cdot E + [M] \cdot H$, where M is the matrix

$$[M] = \begin{bmatrix} 0 & -\frac{\sigma_z''(z)/i\omega}{\sigma_z'(z)+i\omega} & 0 \\ \frac{\sigma_z''(z)/i\omega}{\sigma_z'(z)+i\omega} & 0 & 0 \\ 0 & 0 & 0 \end{bmatrix}. \tag{87}$$

Moreover, when $\sigma_z''(z) = 0$, Eq. (86) is the same as Eq. (81). In that case only, system (86) admits both the unbounded solutions in Eqs. (82)–(83) and the bounded solutions in Eq. (84)–(85), as $\omega \to 0$. Clearly, the physical solutions are the bounded ones. Thus, we show that if the strength of the uniaxial absorbing medium is constant, it admits decaying plane waves that are uniformly bounded, while in previous papers, there was always an unbounded scaling factor associated with the solution in the uniaxial medium.

In a numerical implementation an on/off switch can be used to drop the lower-order terms in the left-hand side of (86), i.e., zero the M matrix, thus allowing us to compare the biaxial and uniaxial approaches on a given problem with a given conductivity profile in the layer. Also, a varying-profile uniaxial PML can also be viewed as a series of constant-profile uniaxial PML's. This, together with its simpler formulation, suggests that the uniaxial PML may have a better performance in numerical experiments. We note here that [10] gives a uniaxial PML in rectangular coordinates whose plane-wave solutions are uniformly bounded for a variable conductivity uniaxial PML, but the damping properties of that layer depend on ω and one no longer obtains frequency-independent damping of propagating waves. Also, the time-domain form of [10] is computationally more expensive than the standard unsplit PML which they erroneously prove to be noncausal. We desire to maintain the frequency-independent damping for the bounded solutions and therefore we develop the biaxial unsplit PML.

A direct application of the uniaxial medium idea in spherical and cylindrical coordinate systems was presented in [9], where analysis of the reflection and absorption of cylindrical and spherical waves in the medium was given. Some restrictions and problems with this direct application of Sacks' anisotropic medium idea in those coordinate systems were observed. Kuzuoglu and Mittra obtained the spherical and cylindrical wave solutions in the medium and their reflection coefficients at vacuum–layer interface. These authors observed that the medium was not ideally nonreflecting anymore and showed that it could effectively absorb waves without reflection only under the condition that the radius of the vacuum–layer interface is electrically large.

In the following, we discuss the biaxial and the uniaxial medium PML methods which are ideally nonreflecting at the vacuum–layer interface in spherical and cylindrical coordinates. These extensions are different from those proposed in [9], of course. The relation between the biaxial and the uniaxial medium PML methods in spherical or cylindrical coordinates is the same as that in Cartesian coordinates. The biaxial PML method admits plane-wave

solutions that are uniformly bounded and can be reduced to the uniaxial PML method by choosing the spatial variation of the damping or by dropping the extra source terms as described above. For conciseness, we will not give the equations or the solutions for the uniaxial PML methods separately.

4.2. *Anisotropic Spherical PML Methods*

In this section we give the equations and solutions of the anisotropic spherical PML methods. The methods, by construction, are symmetric hyperbolic and strongly well-posed. For this well-posed spherical PML method, the following plane-wave solution is what we desired in the layer,

$$\tilde{H}_r = H_r D(r,\theta,\phi), \tag{88}$$

$$\tilde{H}_\theta = \frac{\frac{\sigma_r(r)}{r} + i\omega}{\sigma_r'(r) + i\omega} H_\theta D(r,\theta,\phi), \tag{89}$$

$$\tilde{H}_\phi = \frac{\frac{\sigma_r(r)}{r} + i\omega}{\sigma_r'(r) + i\omega} H_\phi D(r,\theta,\phi), \tag{90}$$

where H_r, H_ϕ, and H_θ are plane-wave solutions of the original Maxwell's equations and

$$D(r,\theta,\phi) = e^{-\sigma_r(r)(\cos\theta_0\cos\theta + \sin\theta_0\sin\theta\cos(\phi-\phi_0))} \tag{91}$$

is the decaying factor. $\tilde{E}_r$, $\tilde{E}_\phi$, and $\tilde{E}_\theta$ are defined similarly. Let the vacuum–layer interface be at $r = r_0$. We require that $\sigma_r(r) = 0$ for $r \le r_0$ for the decaying plane waves in the PML to match incident plane waves perfectly. Following the considerations of the absorbing and reflectionless properties of the polar PML method, $\sigma_r(r)$ must satisfy the same conditions as those in Eqs. (45)–(47). Thus the decaying plane-wave solutions are perfectly matched with the free-space plane-wave solutions. For the type of function $\sigma_r(r)$ we use, one notes that

$$\frac{\sigma_r(r)}{r} < \sigma_r'(r) \tag{92}$$

holds for all $r > r_0$. Hence, the above plane-wave solutions are uniformly bounded.

LEMMA 4.1.

$$\frac{1}{r\sin\theta}\frac{\partial \tilde{H}_r}{\partial\phi} - \frac{\partial \tilde{H}_\phi}{\partial r} - \frac{\tilde{H}_\phi}{r} - \sigma_r''(r)\frac{\tilde{H}_\phi}{\sigma_r'(r)+i\omega} = \frac{\frac{\sigma_r(r)}{r}+i\omega}{i\omega} D(r,\theta,\phi)\frac{\partial E_\phi}{\partial t}. \tag{93}$$

Proof. We have

$$\begin{aligned}
&\frac{1}{r\sin\theta}\frac{\partial \tilde{H}_r}{\partial\phi} - \frac{\partial \tilde{H}_\phi}{\partial r} - \frac{\tilde{H}_\phi}{r} - \sigma_r''(r)\frac{\tilde{H}_\phi}{\sigma_r'(r)+i\omega} \\
&= \frac{\frac{\sigma_r(r)}{r}+i\omega}{i\omega}\left(\frac{1}{r\sin\theta}D\frac{\partial H_r}{\partial\phi} - \frac{1}{r}DH_\phi\right) - \frac{\frac{\sigma_r(r)}{r}+i\omega}{i\omega}\left(D\frac{\partial H_\phi}{\partial r}\right) \\
&\quad + \frac{1}{r}DH_\phi - \frac{\frac{\sigma_r(r)}{r}+i\omega}{\sigma_r'(r)+i\omega}\frac{1}{r}DH_\phi - \sigma_r''(r)\frac{\tilde{H}_\phi}{\sigma_r'(r)+i\omega} - \left(\frac{\frac{\sigma_r(r)}{r}+i\omega}{\sigma_r'(r)+i\omega}\right)' DH_\phi
\end{aligned}$$

$$
\begin{aligned}
&= \frac{\frac{\sigma_r(r)}{r} + i\omega}{i\omega}\left(\frac{1}{r\sin\theta}D\frac{\partial H_r}{\partial\phi} - \frac{1}{r}DH_\phi - D\frac{\partial H_\phi}{\partial\phi}\right)\\
&\quad + \frac{\sigma_r' - \frac{\sigma_r}{r}}{\sigma_r' + i\omega}\frac{1}{r}DH_\phi - \frac{\left(\frac{\sigma_r}{r}\right)'}{\sigma_r' + i\omega}DH_\phi + \frac{\sigma_r''}{\sigma_r' + i\omega}\tilde{H}_\phi - \sigma_r''(r)\frac{\tilde{H}_\phi}{\sigma_r'(r) + i\omega}\\
&= \frac{\frac{\sigma_r(r)}{r} + i\omega}{i\omega}D(r,\theta,\phi)\left(\frac{1}{r\sin\theta}\frac{\partial H_r}{\partial\phi} - \frac{\partial H_\phi}{\partial r} - \frac{H_\phi}{r}\right).
\end{aligned}
$$

Hence Eq. (93) holds. ■

Remark 4.1. Similarly, we can prove other relations that are needed to obtain the equations that admit the desired set of solutions, e.g.,

$$
\frac{\partial\tilde{H}_\theta}{\partial r} - \frac{1}{r}\frac{\partial\tilde{H}_r}{\partial\theta} + \frac{\tilde{H}_\theta}{r} + \sigma_r''(r)\frac{\tilde{H}_\phi}{\sigma_r'(r) + i\omega} = \frac{\frac{\sigma_r(r)}{r} + i\omega}{i\omega}D(r,\theta,\phi)\frac{\partial E_\theta}{\partial t}. \tag{94}
$$

The guiding principle of the construction is to maintain the principal part of Maxwell's equations unchanged.

In obtaining the set of equations that admit the desired solutions, we add complementary source terms to the original Maxwell's equations. Let us denote

$$
Bi_r = \sigma_r''(r). \tag{95}
$$

We first give the equations in the frequency-domain:

$$
\frac{\left(\frac{\sigma_r(r)}{r} + i\omega\right)^2}{\sigma_r'(r) + i\omega}\tilde{E}_r = \frac{1}{r\sin\theta}\frac{\partial}{\partial\theta}(\sin\theta(\tilde{H}_\phi)) - \frac{1}{r\sin\theta}\frac{\partial\tilde{H}_\theta}{\partial\phi}, \tag{96}
$$

$$
(i\omega + \sigma_r'(r))\tilde{E}_\theta = \frac{1}{r\sin\theta}\frac{\partial\tilde{H}_r}{\partial\phi} - \frac{\partial\tilde{H}_\phi}{\partial r} - \frac{\tilde{H}_\phi}{r} - Q_H, \tag{97}
$$

$$
(i\omega + \sigma_r'(r))\tilde{E}_\phi = \frac{\partial\tilde{H}_\theta}{\partial r} - \frac{1}{r}\frac{\partial\tilde{H}_r}{\partial\theta} + \frac{\tilde{H}_\theta}{r} + R_H. \tag{98}
$$

The supplementary fields have the solutions:

$$
Q_H = \frac{Bi_r}{\sigma_r'(r) + i\omega}\tilde{H}_\phi, \tag{99}
$$

$$
R_H = \frac{Bi_r}{\sigma_r'(r) + i\omega}\tilde{H}_\theta. \tag{100}
$$

To verify Eq. (96), one needs to notice that

$$
\frac{1}{r\sin\theta}\frac{\partial}{\partial\theta}(\sin\theta(\tilde{H}_\phi)) - \frac{1}{r\sin\theta}\frac{\partial\tilde{H}_\theta}{\partial\phi} = \frac{\frac{\sigma_r(r)}{r} + i\omega}{\sigma_r'(r) + i\omega}\frac{\partial\tilde{E}_r}{\partial t}. \tag{101}
$$

To verify Eq. (97) and Eq. (96), one needs to apply Eq. (93) and Eq. (94), respectively. Evolution equations for H_r, H_θ, and H_ϕ can be similarly obtained.

To obtain the time-domain equations, we let

$$\bar{E}_r = \frac{\frac{\sigma_r(r)}{r} + i\omega}{\sigma_r'(r) + i\omega}\tilde{E}_r, \tag{102}$$

$$\bar{H}_r = \frac{\frac{\sigma_r(r)}{r} + i\omega}{\sigma_r'(r) + i\omega}\tilde{H}_r, \tag{103}$$

and denote

$$D_E = \tilde{E}_r - \bar{E}_r, \quad D_H = \tilde{H}_r - \bar{H}_r. \tag{104}$$

We obtain the set of equations that is symmetric hyperbolic, from which the well-posedness follows,

$$\begin{aligned}\frac{\partial \tilde{E}_r}{\partial t} &+ \left(\frac{2\sigma_r(r)}{r} - \sigma_r'(r)\right)\tilde{E}_r \\ &= \frac{1}{r\sin\theta}\frac{\partial}{\partial\theta}(\sin\theta(\tilde{H}_\phi)) - \frac{1}{r\sin\theta}\frac{\partial \tilde{H}_\theta}{\partial\phi} + \left(\frac{\sigma_r(r)}{r} - \sigma_r'(r)\right)D_E,\end{aligned} \tag{105}$$

$$\frac{\partial \tilde{E}_\theta}{\partial t} + \sigma_r'(r)\tilde{E}_\theta = \frac{1}{r\sin\theta}\frac{\partial \tilde{H}_r}{\partial\phi} - \frac{\partial \tilde{H}_\phi}{\partial r} - \frac{\tilde{H}_\phi}{r} - Q_H, \tag{106}$$

$$\frac{\partial \tilde{E}_\phi}{\partial t} + \sigma_r'(r)\tilde{E}_\phi = \frac{\partial \tilde{H}_\theta}{\partial r} - \frac{1}{r}\frac{\partial \tilde{H}_r}{\partial\theta} + \frac{\tilde{H}_\theta}{r} + R_H, \tag{107}$$

and the supplementary ordinary differential equations are given in the following:

$$\frac{\partial D_E}{\partial t} = \left(\sigma_r'(r) - \frac{\sigma_r}{r}\right)\tilde{E}_r - \sigma_r'(r)D_E, \tag{108}$$

$$\frac{\partial Q_H}{\partial t} = Bi_r\tilde{H}_\phi - \sigma_r'(r)Q_H, \tag{109}$$

$$\frac{\partial R_H}{\partial t} = Bi_r\tilde{H}_\phi - \sigma_r'(r)R_H. \tag{110}$$

As in the Cartesian case, one can reduce the biaxial PML to the uniaxial PML method either by dropping the extra source terms, i.e., setting Bi_r to zero with a switch, or by choosing a linear loss profile in the layer. Then, Q_H and R_H become zero and the governing ODEs are not needed. A set of uniaxial plane-wave solutions for a varying uniaxial PML, i.e. $\sigma_r''(r)$ not identically zero, can be obtained by multiplying the biaxial plane-wave solutions by $(\sigma_r'(r) + i\omega)/i\omega$. The whole scenario is very similar to that in the Cartesian case.

In the frequency domain, the uniaxial PML equations obtained from Eqs. (96)–(98) are essentially the same as the ones proposed by Teixeira and Chew in [16], and the ones proposed by Petropoulos in [17]. However, the time-domain equations in [16] are different and there are no numerical experiments presented.

The above supplementary fields exhibit some properties that have been found useful in numerical computation. One notes that $\tilde{E}_r - D_E = \bar{E}_r$, $\tilde{H}_r - D_E = \bar{H}_r$, and the fields $\bar{E}_r$, $\tilde{E}_\theta$, and $\tilde{E}_\phi$ have the same scaling factor, $\sigma_r(r)/r + i\omega/\sigma_r'(r) + i\omega$. One also notes that all the supplementary fields are zero at the vacuum–layer interface. In fact, the above formulation of the spherical PML method is obtained by fine-tuning the formulation of the auxiliary

fields and auxiliary equations. The final formulation is found to have the best accuracy and robustness in numerical experiments, besides having the property of being symmetric hyperbolic.

In our multidomain computational scheme simulating the spherical PML, we apply a locally rotated coordinate system in subdomains near north and south poles to avoid the $1/\sin\theta$ singularity. Hence we want to transform forward and backward between (E_x, E_y, E_z) and (E_r, E_θ, E_ϕ) to patch the fields. Note that this needs to be done at the subdomain interfaces of the rotated subdomains only. In our scheme, we make use of the fact that the supplementary fields are zero at the vacuum–layer interface. The details of the implementation will be given elsewhere.

4.3. *Anisotropic Cylindrical PML Methods*

Finally, we give the anisotropic PML methods in cylindrical coordinates. For the anisotropic cylindrical PML method, the following plane-wave solution is what we desire in the layer:

$$\tilde{E}_\rho = \frac{i\omega}{\sigma_z'(z) + i\omega} E_\rho D(\rho, \phi, z), \tag{111}$$

$$\tilde{E}_\phi = \frac{i\omega}{\sigma_z'(z) + i\omega} \frac{\frac{\sigma_\rho(\rho)}{\rho} + i\omega}{\sigma_\rho'(\rho) + i\omega} E_\phi D(\rho, \phi, z), \tag{112}$$

$$\tilde{E}_z = \frac{i\omega}{\sigma_z'(\rho) + i\omega} E_z D(\rho, \phi, z), \tag{113}$$

where E_ϕ, E_θ, H_ϕ, and H_θ are plane-wave solutions in Eqs. (20)–(22) and

$$D(\rho, \phi, z) = e^{-\sigma_\rho(\rho)\sqrt{1-n^2}\cos(\phi-\phi_0) - \sigma_z(z)nz} \tag{114}$$

is the decay factor. Let the vacuum–layer interface be at $\rho = \rho_0$ and $|z| = z_0$. We require that $\sigma_\rho(\rho) = 0$ for $\rho \le \rho_0$ and $\sigma_z(z) = 0$ for $|z| \le z_0$ in order for the decaying plane-waves in the PML to match incident plane-waves perfectly. Following the considerations of the absorbing and reflectionless properties of the polar PML method, $\sigma_\rho(\rho)$ and $\sigma_z(z)$ must satisfy the same conditions as those in the Eqs. (65)–(66). Thus, the solutions are perfectly matched with the free-space plane-wave solutions. One can easily see that the above plane-wave solutions are uniformly bounded like those in Cartesian and spherical coordinate systems.

To get a set of equations that admit the above solutions, we add complementary source terms to the original Maxwell's equations. The evolution of these source terms is governed by ordinary differential equations. Let us denote

$$Bi_\rho = \sigma_\rho''(\rho), \quad Bi_z = \sigma_z''(z). \tag{115}$$

We then have the following system of equations for the cylindrical PML:

$$\frac{\partial \tilde{E}_\rho}{\partial t} + \left(\sigma_z'(z) + \frac{\sigma_\rho(\rho)}{\rho} - \sigma_\rho'(\rho)\right)\tilde{E}_\rho + \left(\frac{\sigma_\rho(\rho)}{\rho} - \sigma_\rho'(\rho)\right)(\sigma_z'(z) - \sigma_\rho'(\rho))P_E = \frac{1}{\rho}\frac{\partial \tilde{H}_z}{\partial \phi} - \frac{\partial \tilde{H}_\phi}{\partial z} - Bi_z T_H, \tag{116}$$

$$\frac{\partial \tilde{E}_\phi}{\partial t} + \left(\sigma_z'(z) + \sigma_\rho'(\rho) - \frac{\sigma_\rho(\rho)}{\rho}\right)\tilde{E}_\rho + \left(\sigma_\rho'(\rho) - \frac{\sigma_\rho(\rho)}{\rho}\right)\left(\sigma_z'(z) - \frac{\sigma_\rho(\rho)}{\rho}\right) Q_E$$
$$= \frac{\partial \tilde{H}_\rho}{\partial z} - \frac{\partial \tilde{H}_z}{\partial \rho} + Bi_z U_H - Bi_\rho V_H, \tag{117}$$

$$\frac{\partial \tilde{E}_z}{\partial t} + \left(\frac{\sigma_\rho(\rho)}{\rho} + \sigma_\rho'(\rho) - \sigma_z'(z)\right)\tilde{E}_z + (\sigma_\rho'(\rho) - \sigma_z'(z))\left(\frac{\sigma_\rho(\rho)}{\rho} - \sigma_z'(z)\right) R_E$$
$$= \frac{\partial \tilde{H}_\phi}{\partial \rho} - \frac{1}{\rho}\frac{\partial \tilde{H}_\rho}{\partial \phi} + \frac{\tilde{H}_\phi}{\rho} + Bi_\rho W_H, \tag{118}$$

and the supplementary ordinary differential equations are given as

$$\frac{\partial P_E}{\partial t} = \tilde{E}_\rho - \sigma_\rho'(\rho) P_E, \tag{119}$$
$$\frac{\partial Q_E}{\partial t} = \tilde{E}_\phi - \frac{\sigma_\rho(\rho)}{\rho} Q_E, \tag{120}$$
$$\frac{\partial R_E}{\partial t} = \tilde{E}_z - \sigma_z(z) R_E, \tag{121}$$
$$\frac{\partial T_H}{\partial t} = \tilde{H}_\phi - \sigma_z'(z) T_H, \tag{122}$$
$$\frac{\partial U_H}{\partial t} = \tilde{H}_\rho - \sigma_z'(z) U_H, \tag{123}$$
$$\frac{\partial V_H}{\partial t} = \tilde{H}_z - \sigma_\rho'(\rho) V_H, \tag{124}$$
$$\frac{\partial W_H}{\partial t} = \tilde{H}_\phi - \sigma_\rho'(\rho) W_H. \tag{125}$$

Note that the system of equations is symmetric hyperbolic and, hence, strongly well-posed. The supplementary fields are similar to those in the spherical case in formulation and can be obtained without much difficulty. As in the Cartesian case, we can reduce the biaxial PML to the uniaxial PML by setting Bi_ρ and Bi_z to be zero or by choosing a linear loss profile in the layer. Then T_H, U_H, V_H, and W_H are not needed in the PDE. Hence, in that case, we do not need to solve Eqs. (122)–(125), and that makes the uniaxial PML computationally less expensive.

5. NUMERICAL EXPERIMENTS

The numerical method we use is a multidomain Chebyshev pseudospectral scheme. As a pseudospectral scheme is infinite-order accurate for smooth solutions, we expect it to be the best underlying scheme for the testing of PMLs. In testing the PMLs we want the numerical reflection due to the PMLs, which is very small, to be fully manifested in the error of numerical solutions.

The computational domain is decomposed into two layers of subdomains. The PMLs being considered are set up in the outer layer to terminate the computational domains. Detailed description of the 3D multidomain spectral scheme does not fit in here and we hope to report on it in the near future.

5.1. *Simulations with the Spherical PML Methods*

To test the spherical PML methods, we first apply them in the simulation of a model problem for which the exact solution is known. The problem is the same as that in [19], where an off-centered radiating electric dipole located at $S = (0, 0, z_0)$, $z_0 > 0$, is considered. Its time dependence is a Gaussian pulse centered at $t = t_0$ [19].

Unlike [19], we simulate the problem in 3D to test the spherical PML methods, although the computational region can be reduced to a 2D region due to inherent symmetry. We decompose the computational domain into 48 subdomains, where the computational mesh we use in each subdomain is $12 \times 12 \times 12$. Half of the subdomains are in the outer layer, i.e., in the PML. The inner boundary of the computational domain is at $r = 0.5[m]$, while the PML layers start at $r = 1.0[m]$. We set $z_0 = 0.4[m]$ in our simulations. We shall compare the numerical solutions with the exact solutions at three different locations well inside the computational domain: $P_1(\theta = 45^\circ, \phi = 0^\circ, r = 0.75[m])$, $P_2(\theta = 90^\circ, \phi = 0^\circ, r = 0.75[m])$, and $P_3(\theta = 180^\circ, \phi = 0^\circ, r = 0.75[m])$.

In Fig. 1, we plot the ϕ-component of the magnetic field versus time at the locations P_1 and P_2, computed with the split-field spherical PML method, on top of the exact solutions. The numerical errors at the two locations are very small. After the pulse passes, the maximum residual amplitude is only 0.1% of the exact solutions approximately. Note

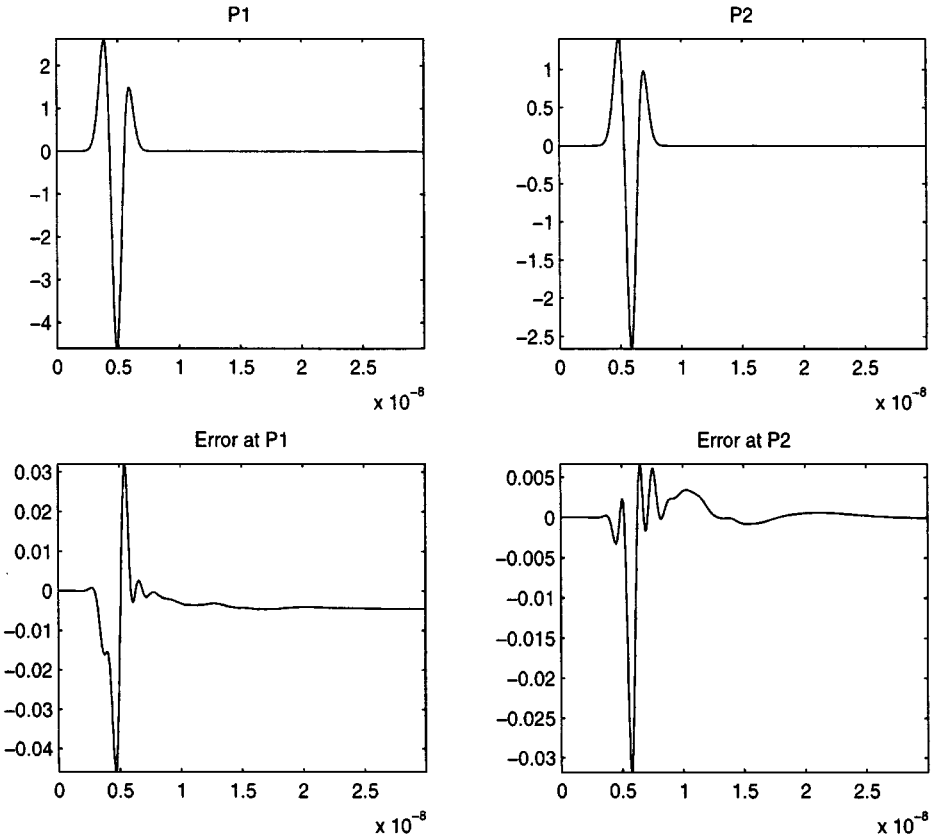

FIG. 1. The numerical solution of H^ϕ at P_1 and P_2 (dashed lines), computed using the split-field spherical PML method, is compared with the exact solution (solid line).

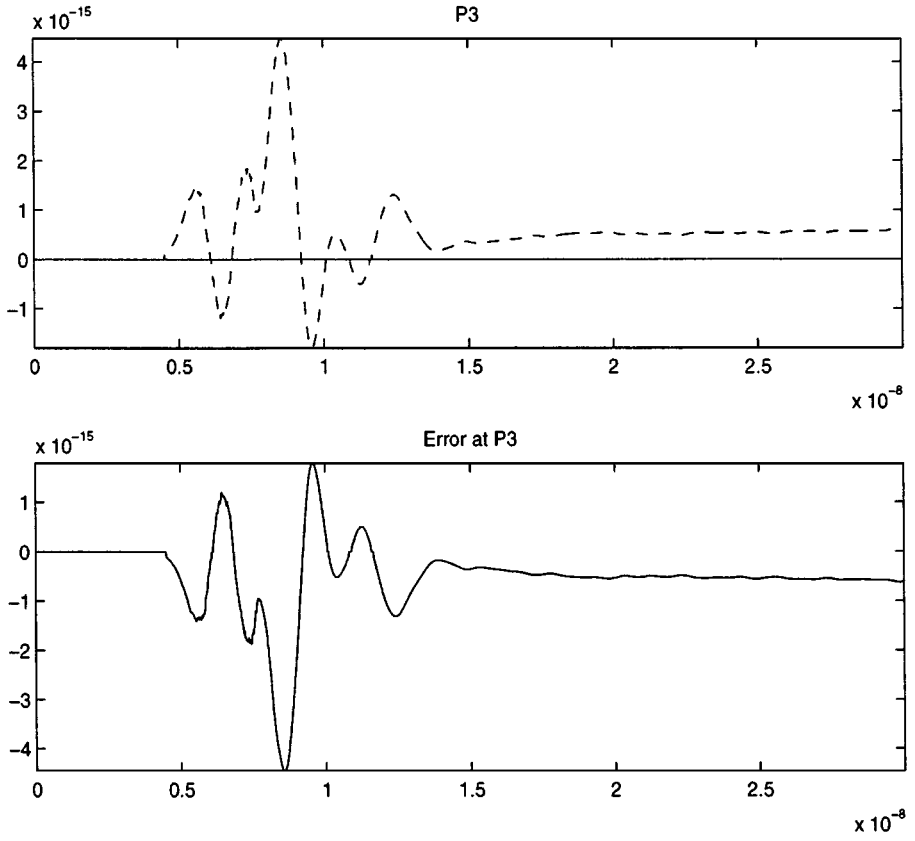

FIG. 2. The numerical solution of H^{ϕ} at P_3 (dashed line), computed using the split-field spherical PML method, is compared with the exact solution (solid line).

that when the pulse passes the location, there is no reflection coming from the boundary since the wave has not yet reached the PML region. The error at that stage is solely due to the discretization error of the sharp pulse. In Fig. 2, we plot the ϕ-component of the magnetic field at point P_3, computed with the same method, on top of the exact solution which is zero at P_3. One notes that the error is as low as $5.0E-15$, which strongly suggests that reflections are absorbed locally and do not contaminate the solution elsewhere.

In Fig. 3, we plot the ϕ-component of the magnetic field versus time at the locations P_1 and P_2, computed with the uniaxial spherical PML method, on top of the exact solutions. One notes that the reflection of the PML is also very small, less than 0.1% of the exact solution. The ϕ-component of the magnetic field at point P_3, computed with the same method, is also extremely small like in Fig. 2, which strongly suggests that the numerical error is absorbed locally and does not contaminate the solution elsewhere.

In Fig. 4, we plot the ϕ-component of the magnetic field versus time at the locations P_1 and P_2, computed with the biaxial spherical PML method, on top of the exact solutions. One notes that the reflection from the PML is again very small, less than 0.1% of the exact solution. The ϕ-component of the magnetic field at point P_3, computed with the same method, is also extremely small like in Fig. 2, which strongly suggests that the numerical error is absorbed locally and does not contaminate the solution elsewhere.

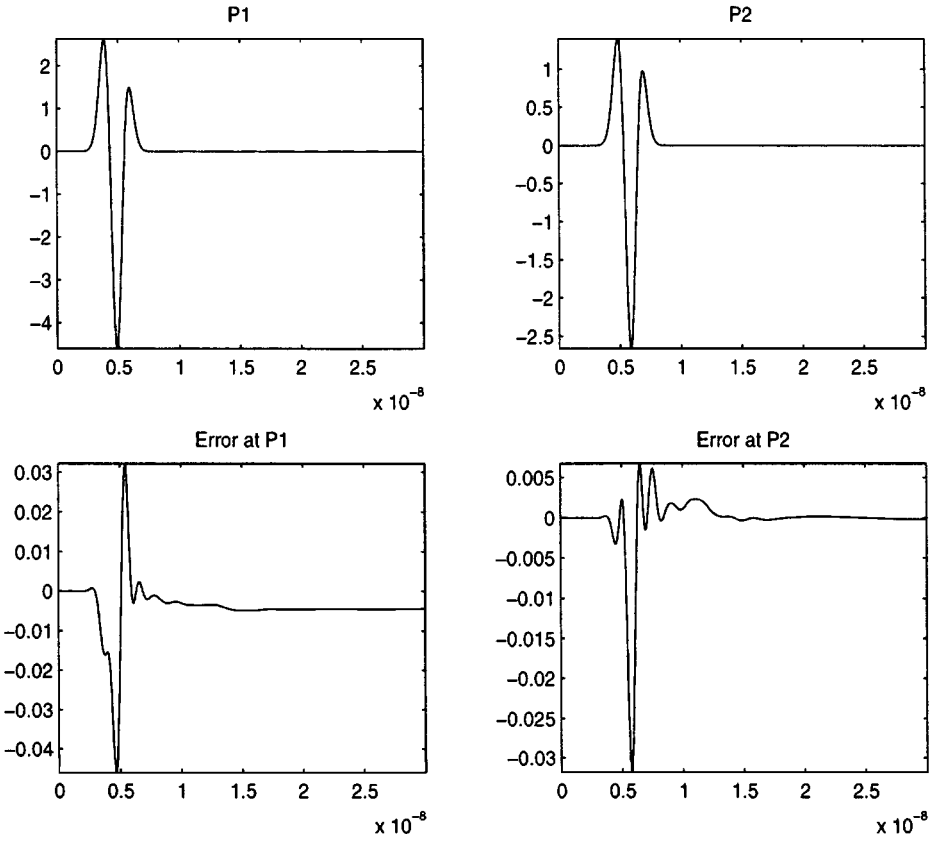

FIG. 3. The numerical solution of H^{ϕ} at P_1 and P_2 (dashed lines), computed using the uniaxial spherical PML method, is compared with the exact solution (solid line).

In Fig. 5, we compare the error history of different spherical PML methods. The discrete L_2 error is computed on all the grid points in the inner subdomain and plotted versus time with the field normalized. Numerical results show that the accuracy of the three types of PML methods are very close.

Finally, in Fig. 6 we compare the split-field and the uniaxial PMLs for a dipole whose amplitude as a function of time is a smoothed step function, i.e., for a source with significant $\omega = 0$ frequency content. As expected, both methods fail for this case; however, the overall error history of the uniaxial PML is much better than that of the split-field PML. The latter is better at an early stage but diverges eventually. It appears that the underlying problem with the two methods is different. The result of the biaxial PML, which is close to, but not as good as, that of the uniaxial PML, is omitted here. One unsolved problem with biaxial PML in time domain is that when $\omega = 0$, supplementary fields such as Q_H and R_H are unbounded at the vacuum–layer interface $r = r_0$. However, the biaxial PML does not have this problem in frequency domain and the situation should be different in frequency domain. In the constant profile case, the time-domain uniaxial PML method we propose only needs supplementary fields D_H and D_E that are uniformly bounded. Indeed, all fields are bounded in this case. These issues are currently under investigation. Note that the simulation time in this test is an order of magnitude larger than that of the previous tests.

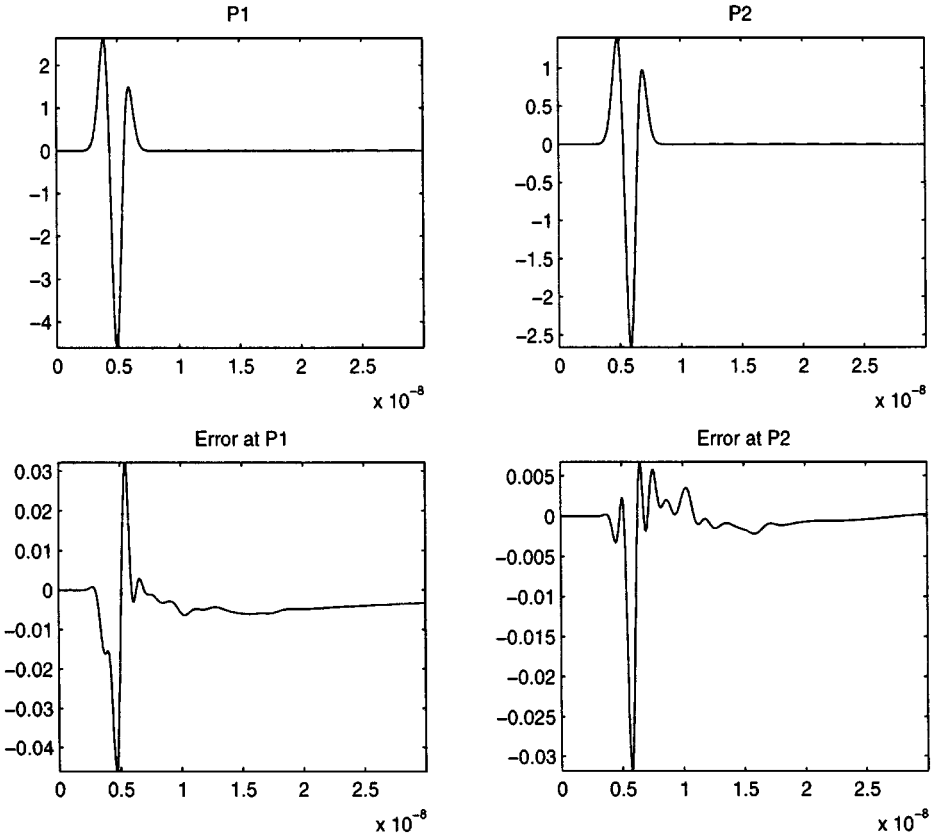

FIG. 4. The numerical solution of H^{ϕ} at P_1 and P_2 (dashed lines), computed using the biaxial spherical PML method, is compared with the exact solution (solid line).

We have also simulated scattering by a PEC sphere. In this simulation, we used 12 subdomains, and in each subdomain a $16 \times 16 \times 16$ grid is used. The split-field PML, the biaxial PML, and the uniaxial PML methods were all used to truncate the simulation, and the Mie-series result was taken as the RCS reference. To determine the size of the reflection of the perfectly matched layers, we also compare the computed fields to those computed using a larger computational domain.

In Fig. 7 we present the RCS result of scattering by a PEC sphere of electrical size $ka = 5.3$, with the Mie-series RCS result as the reference. Here we use the multidomain pseudospectral method with the split-field, uniaxial, and biaxial spherical PMLs. All three approaches give very accurate results, within 0.01–0.02 db of the exact one. The results from all the methods are again very close.

In Fig. 8 we plot, versus time, the E_x field $\lambda/2$ from the scatterer surface in the back scatter region, and the difference between the field and the one obtained in the reference computation using a larger computational domain. It is shown in the figure that the difference between the two fields is within 1×10^{-3} after the initial noise, which is the result of the initial nonsmoothness of the type of excitation used. Due to resource restrictions, we could not run this test for a longer time. However, our 2D tests in [3, 4] suggest that the reflection of PML methods remain this low even after a much longer time.

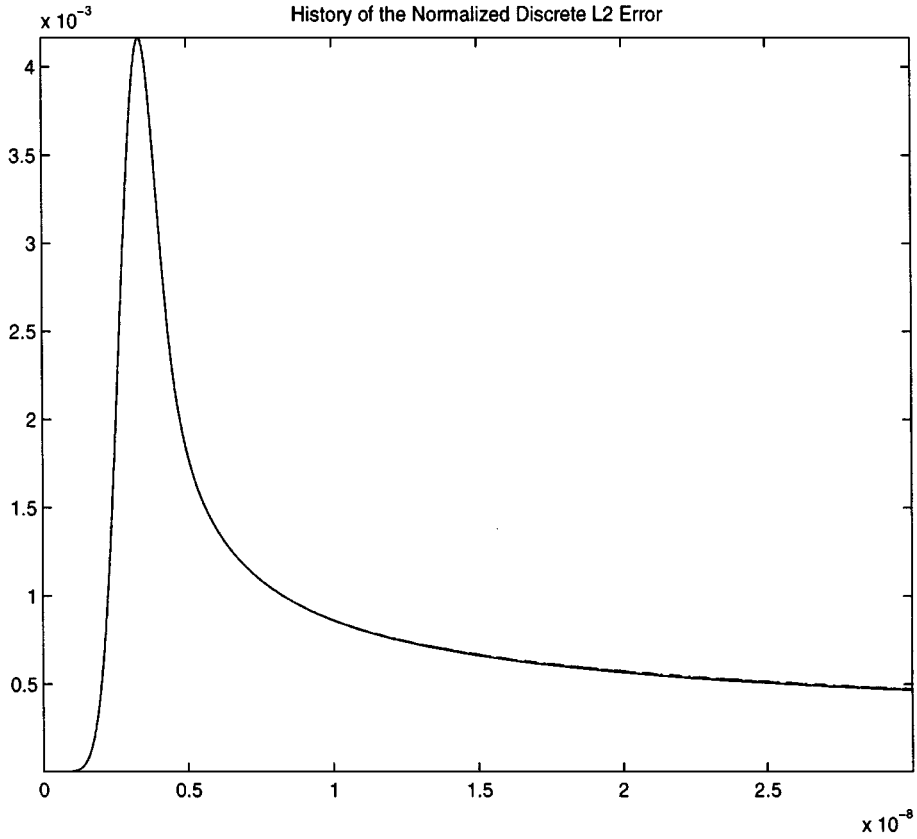

FIG. 5. History of the normalized discrete L_2 error of the split-field spherical PML (dash-dotted line), the uniaxial spherical PML (dashed line), and the biaxial spherical PML (solid line).

5.2. *Simulations with the Cylindrical PML Methods*

The cylindrical PML methods are similar in nature to the polar PML methods in 2D and the spherical PML methods in 3D. Hence, we shall only simulate electromagnetic scattering by a finite-height perfectly conducting cylinder to validate our methods. For reference, we scanned and measured the MOM results in [18].

In Fig. 9 we present the RCS result of a finite PEC cylinder of radius 2λ and height 2λ. Our result is obtained with the multidomain pseudospectral method using the split-field cylindrical perfectly matched layer as the absorbing boundary condition. We employ two layers of subdomains to surround the cylinder, with 18 subdomains in each layer. As usual, a cylindrical PML is put in the outer layer. In each subdomain, the computational grid used is $16 \times 16 \times 16$. Note that the numerical result is in good agreement with the reference.

We also run the same problem with the uniaxial and biaxial cylindrical PMLs as the absorbing boundary conditions. Similarly to the split-field cylindrical PML case, these numerical results were in good agreement with the reference. Due to the fact that the uniaxial cylindrical PML method requires a smaller number of additional equations to solve than the biaxial cylindrical PML method, the uniaxial cylindrical PML seems to be a better choice for high-frequency problems.

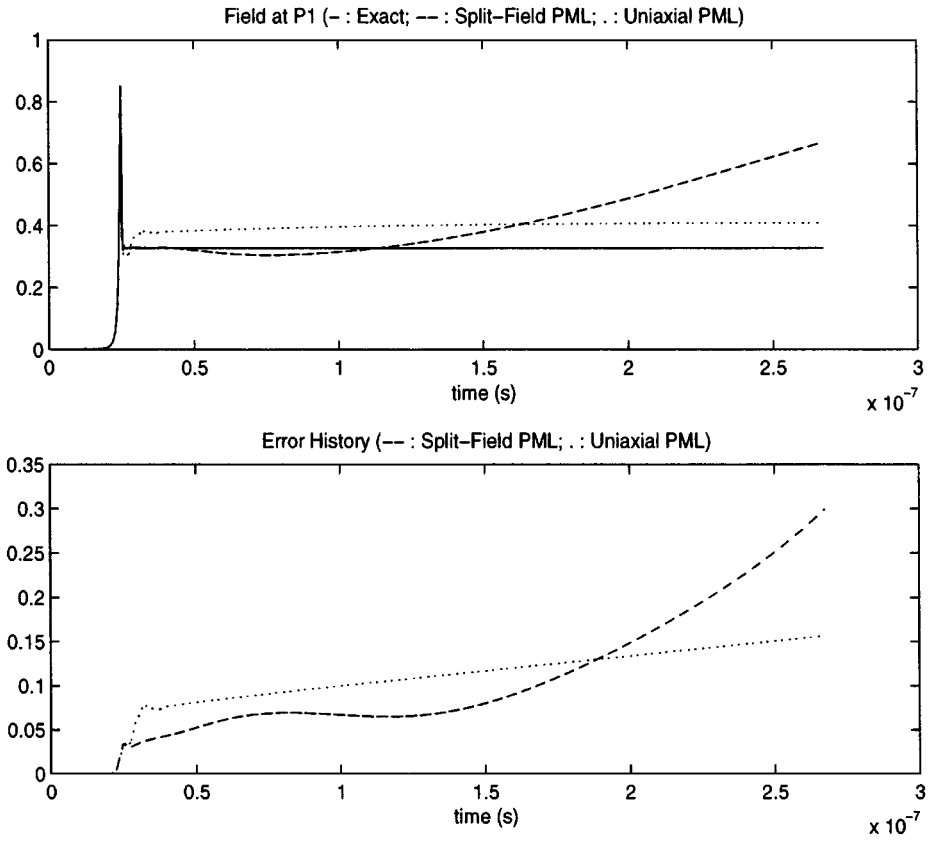

FIG. 6. The numerical solution of E_r at P_1 computed using the split-field (dash) and uniaxial (dot) spherical PML methods, is compared with the exact solution (solid line), and the normalized discrete L_2 error of the split-field spherical PML (dash) is compared with that of the uniaxial spherical PML (dot).

6. CONCLUDING REMARKS

In this paper, three types of PML methods are discussed and compared, i.e. the split-field, the biaxial, and the uniaxial PML methods.

The proposed split-field spherical PML has the property of admitting plane-wave solutions that decay in all directions of propagation. The biaxial PML we propose differs from other anisotropic PMLs in that it is shown to admit plane-wave solutions that are uniformly bounded while the fields in the layer decay exponentially independently of the frequency. However, we also show that the uniaxial PML admits uniformly bounded plane-wave solutions when the PML is constant, and the uniaxial PML needs less supplementary equations than the biaxial PML does. For both the biaxial and the uniaxial PML methods, we present here the time-domain equations that have the important property of being symmetric hyperbolic, from which well-posedness follows. The reduction from the biaxial PML into the uniaxial PML can actually be controlled by a switch.

All the PML methods are demonstrated to be effective in numerical experiments and they give very similar numerical results. Reflection from the PMLs is as low as 0.1% of the amplitude of the wave. A detailed presentation of the 3D multidomain spectral method we use and the implementation details of the PML methods, which have a big influence on

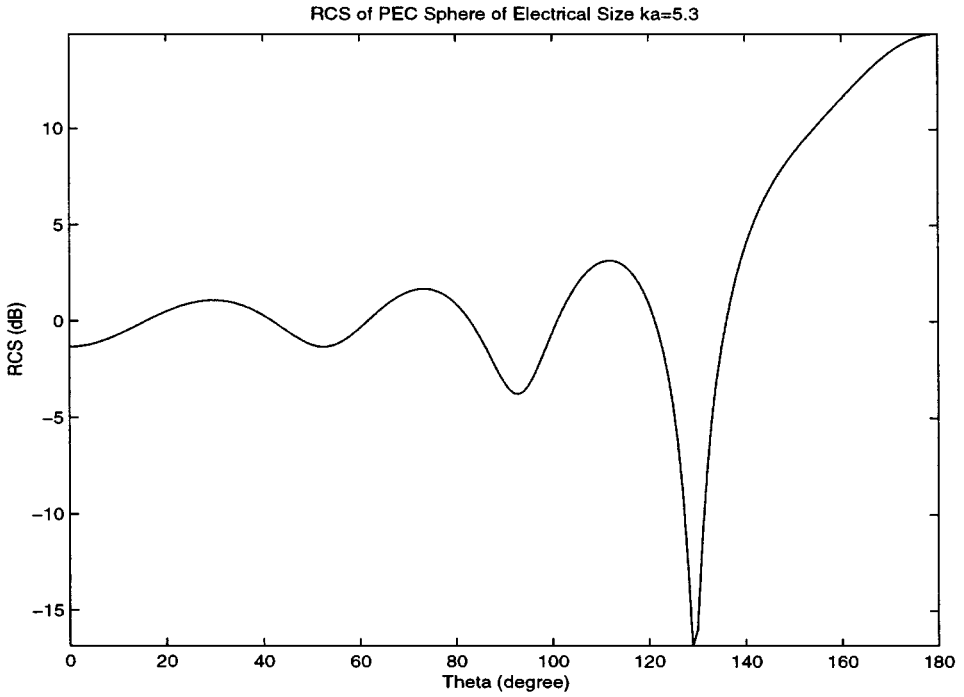

FIG. 7. Plots of RCS's obtained from the pseudospectral method with the split-field spherical PML (dashed line), the uniaxial spherical PML (dash-dotted line), and the biaxial spherical PML (dotted line) on top of the Mie-series RCS (solid line), for a PEC sphere of electrical size $ka = 5.3$.

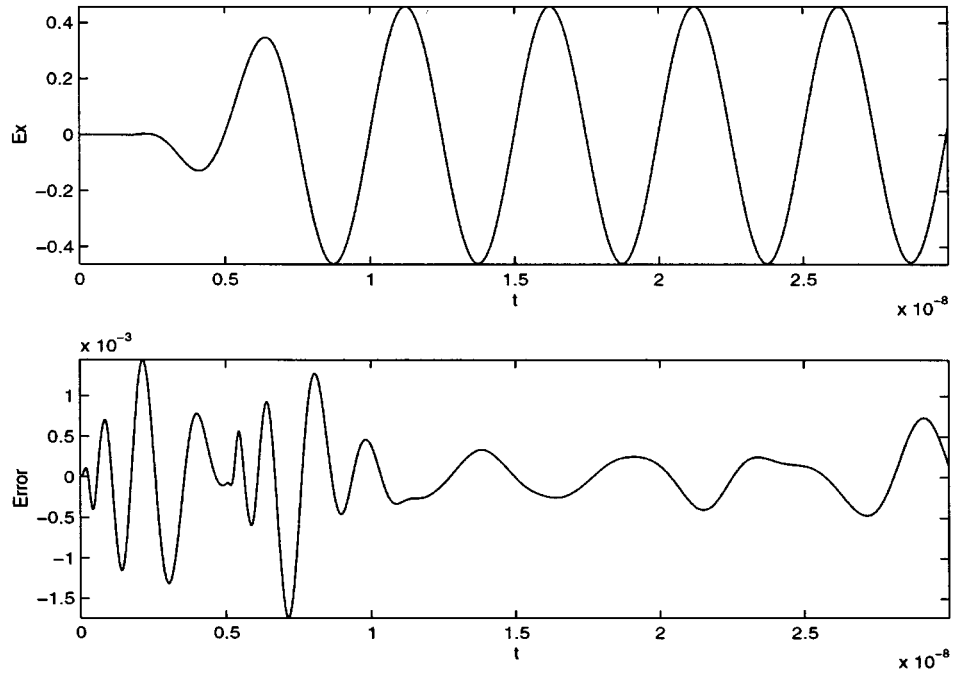

FIG. 8. Comparison of field obtained from spectral method with split-field spherical PML, dashed line, and reference, solid line, for a PEC sphere with electrical size $ka = 5.3$.

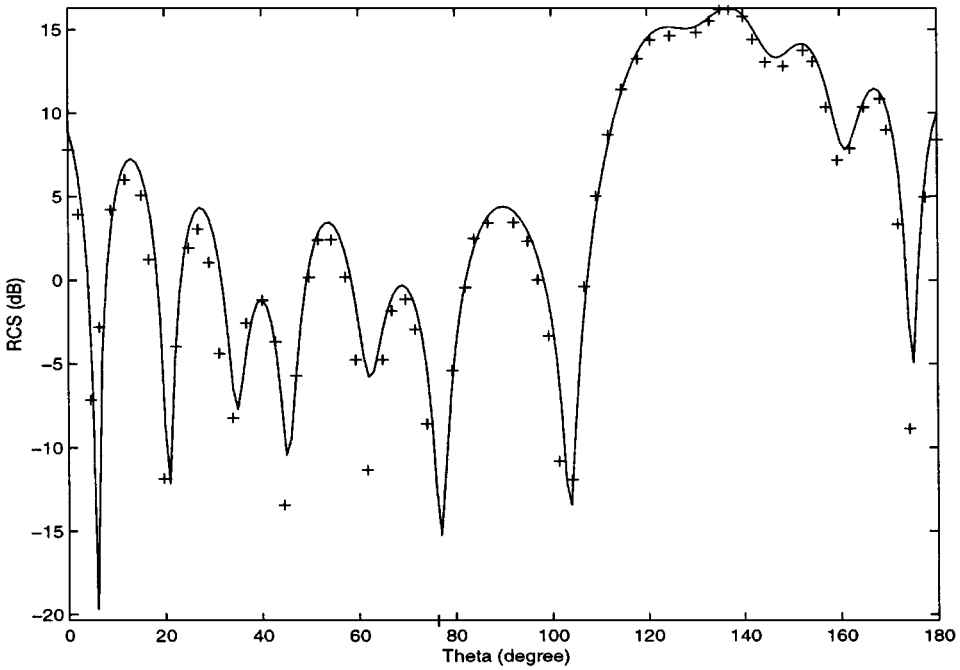

FIG. 9. Comparison of RCS's obtained from spectral method with cylindrical PML, solid line, and reference, marked by "+," for a PEC cylinder of radius 2λ and height 2λ, horizontal polarization ($\mathbf{E}^{\text{inc}} = \hat{\theta} \cdot E_\theta$, $\theta^{\text{inc}} = \pi/4$, $\phi^{\text{inc}} = \pi/2$, $\phi^{\text{obs}} = \pi/3$).

the results, have to be omitted herein for conciseness, and we hope to report on them in the near future.

Due to the fact that the uniaxial medium PML's time-domain equations is symmetric hyperbolic and has the smallest number of equations, it is the most efficient one to use. What remains to be studied is the boundness of the plane-wave solutions when the PML is not constant.

ACKNOWLEDGMENTS AND DISCLAIMER

The first author would like to thank Professor Marcus J. Grote for his help in setting up the radiating dipole test and Professor Jan Hesthaven for helpful discussions. Both authors are grateful to David Gottlieb for his constant encouragement. The first author was supported by DARPA/AFOSR Grant F49620-96-1-0426. The second author was supported in part by AFOSR Grant F49620-98-1-0001. The U.S. Government is authorized to reproduce and distribute reprints for governmental purposes notwithstanding any copyright notation thereon. The views and conclusions contained herein are those of the author and should not be interpreted as necessarily representing the official policies or endorsements, either expressed or implied, of the Defense Advanced Research Projects Agency, the Air Force Office of Scientific Research, or the U.S. Government.

REFERENCES

1. J.-P. Berenger, A perfectly matched layer for the absorption of electromagnetic waves, *J. Comput. Phys.* **114**, 185 (1994).
2. J.-P. Berenger, Three-dimensional perfectly matched layer for the absorption of electromagnetic waves, *J. Comput. Phys.* **127**, 363 (1996).

3. B. Yang, D. Gottlieb, and J. S. Hesthaven, Spectral simulations of electromagnetic wave scattering, *J. Comput. Phys.* **134**, 216 (1997).
4. B. Yang, D. Gottlieb, and J. S. Hesthaven, On the use of PML ABC's in spectral time—domain simulations of electromagnetic scattering, in *Proc. 13th Annual Review of Progress in Applied Computational Electromagnetics, 1997.*
5. Q. Qi and T. L. Geers, Evaluation of the perfectly matched layer for computational acoustics, *J. Comput. Phys.* **139**(1), 166 (1998).
6. Z. S. Sacks, D. M. Kingsland, R. Lee, and J.-F. Lee, A perfectly matched anisotropic absorber for use as an absorbing boundary condition, *IEEE Trans. Antennas Propag.* **43**, 1460 (1995).
7. S. D. Gedney, An anisotropic perfectly matched layer-absorbing medium for the truncation of FDTD lattices, *IEEE Trans. Antennas Propag.* **44**, 1630 (1996).
8. L. Zhao and A. C. Cangellaris, GT-PML: Generalized theory of perfectly matched layers and its application to the reflectionless truncation of finite-difference time-domain grids, *IEEE Trans. Microwave Theory Tech.* **44**, 2555 (1996).
9. M. Kuzuoglu and R. Mittra, Investigation of nonplanar perfectly matched absorbers for finite-element mesh truncation, *IEEE Trans. Antennas Propag.* **45**, 474 (1997).
10. M. Kuzuoglu and R. Mittra, Frequency dependence of the constitutive parameters of causal perfectly matched anisotropic absorbers, *IEEE Microwave Guided Wave Lett.* **6**, 447 (1996).
11. S. Abarbanel and D. Gottlieb, A mathematical analysis of the PML method, *J. Comput. Phys.* **134**, 357 (1997).
12. S. Abarbanel and D. Gottlieb, On the construction and analysis of absorbing layers in C.E.M., in *Proc. 13th Annual Review of Progress in Applied Computational Electromagnetics, 1997.*
13. C. M. Rappaport, Perfectly matched absorbing boundary conditions based on anisotropic lossy mapping of space, *IEEE Microwave Guided Wave Lett.* **5**(3), 94 (1995).
14. E. A. Navarro, C. Wu, P. Y. Chung, and J. Litva, Application of PML superabsorbing boundary condition in the non-orthogonal FD-TD method, IEE Electronics Letters Online No: 19941139 (1994).
15. F. L. Teixeira and W. C. Chew, PML-FDTD in cylindrical and spherical grids, *IEEE Microwave Guided Wave Lett.* **7**(9) (1997).
16. F. L. Teixeira and W. C. Chew, Systematic derivation of anisotropic PML absorbing media in cylindrical and spherical coordinates, *IEEE Microwave Guided Wave Lett.* **7**(11) (1997).
17. P. G. Petropoulos, Reflectionless sponge layers as absorbing boundary conditions for the numerical solution of Maxwell's equations in rectangular, cylindrical, and spherical coordinates, *SIAM J. Appl. Math.*, submitted.
18. S. D. Gedney and R. Mittra, The use of the FFT for the efficient solution of the problem of electromagnetic scattering by a body of revolution, *IEEE Trans. Antennas Propagat.* **38**, 313 (1990).
19. M. J. Grote and J. B. Keller, Nonreflecting boundary conditions for Maxwell's equations, *J. Comput. Phys.* **139**, 327 (1998).